JOURNAL OF CATALYSIS 79, 104–117 (1983)

Relationship between Solid State Structure and Catalytic Activity of Rare Earth and Bismuth-Containing Molybdate Ammoxidation Catalysts

JAMES F. BRAZDIL AND ROBERT K. GRASSELLI

The Standard Oil Co. (Ohio), Research Center, 4440 Warrensville Center Rd., Cleveland, Ohio 44128

Received March 2, 1982; revised September 10, 1982

The formation of solid solutions in rare earth and bismuth-containing molybdate catalysts plays a key role in the selective ammoxidation of propylene to acrylonitrile. Solid state structural studies of the $Bi_{2-x}Ce_x(MoO_4)_3$ system reveal that bismuth dissolves readily in the $Ce_2(MoO_4)_3$ lattice which crystallizes in the low-temperature $La_2(MoO_4)_3$ structure, yielding a single-phase material when $x \geq 1$. The solubility of cerium in the $Bi_2(MoO_4)_3$ structure is less extensive, with maximum solubility occurring at $x \simeq 0.2$. Structural substitution of bismuth or cerium by rare earth cations such as La, Pr, Nd, and Y results in lattice parameter changes which indicate that bismuth and cerium cations randomly occupy equivalent positions in Bi–Ce–molybdate solid solutions. Catalytic activity maxima correlate well with phase compositions and occur in the two single phase regions, where there is maximum solubility of bismuth in the cerium molybdate phase and maximum solubility of cerium in the bismuth molybdate phase. A third catalytic maximum is observed in the binary phase region of the two saturated solid solutions and coincides with equal solubility of Ce in the Bi–molybdate phase and Bi in the Ce–molybdate phase. At these three optimum catalyst compositions, maximum interactions exist between the three key catalytic components: Bi (α-H-abstracting element), Ce (oxygen and electron transfer element), and Mo (olefin chemisorption and nitrogen insertion element).

INTRODUCTION

Interest in solid state structural aspects of trivalent metal molybdates, especially the rare earth molybdates, stems from their unique electrical, optical, elastic, magnetic, as well as catalytic properties (*1*). Bismuth molybdate is unique among the trivalent molybdates in its ability to catalyze the oxidation, ammoxidation, and oxidative dehydrogenation of olefins to the corresponding unsaturated aldehydes, nitriles, and diolefins with extremely high selectivities (*2, 3*). In addition, cerium-containing bismuth molybdates are reported to be active catalysts for the selective ammoxidation of propylene to acrylonitrile (*4, 5*). We have undertaken a detailed examination of the mixed bismuth–cerium molybdate system as a model of an effective multicomponent oxidation catalyst.

From X-ray diffraction studies, both α-bismuth molybdate [$Bi_2(MoO_4)_3$] (*6*) and cerium molybdate [$Ce_2(MoO_4)_3$] (*7*) have been shown to crystallize with structures which can be derived from the scheelite ($CaWO_4$) structure. In the ABO_4-type scheelite, the A cation is usually divalent and is eight coordinated by oxygen while the B cation is hexavalent and present as descrete BO_4 tetrahedra in the structure. When molybdates or tungstates of trivalent metal cations crystallize with a scheelite structure, three of the A cations are replaced by two trivalent cations producing a cation vacancy in the structure. Taking α-bismuth molybdate as an example, these trivalent molybdates and tungstates are more accurately written as $Bi_{2/3}\square_{1/3}MoO_4$, where □ represents a vacant cation site.

Rare earth molybdates and tungstates have been shown to crystallize in various modifications of this scheelite-derived structure (*7, 8*). The difference between the structural modifications are a result of the possible ways in which the cations and va-

0021-9517/83/010104-14$03.00/0

cancies can be arranged in the lattice. As Jeitschko points out (*9*), the differences between these structures result from the way in which the cation vacancies are ordered, and from the relative degree of distortion of the lattice from the ideal scheelite structure. In $Bi_2(MoO_4)_3$, the vacancy ordering is such that some of the oxygen atoms are bonded only to one molybdenum cation at a distance of 1.68 Å which corresponds to a Mo=O double bond. This vacancy arrangement does not occur in either the $Eu_2(WO_4)_3$ or $La_2(MoO_4)_3$ structures. It has been suggested that Mo=O double bonds are one of the prerequisites for selective catalytic oxidation (*10*).

The $La_2(MoO_4)_3$ structure is characterized by the presence of three interconnected cation vacancies along the z coordinate which does not exist either in the $Bi_2(MoO_4)_3$ or $Eu_2(WO_4)_3$ structures. In addition, the $La_2(MoO_4)_3$ structure deviates slightly from the ideal scheelite arrangement. In contrast to this, both $Eu_2(WO_4)_3$ and $Bi_2(MoO_4)_3$ contain considerable distortions in the arrangement of the BO_4 tetrahedra. Lanthanum molybdate is further distinguished by its large monoclinic unit cell. The cell volume for $La_2(MoO_4)_3$ is 3103 Å^3 while $Bi_2(MoO_4)_3$ and $Eu_2(WO_4)_3$ have cell volumes of 962 and 944 Å^3, respectively.

In this study we have examined the solid state structural aspects of various rare earth-containing bismuth molybdate catalysts. In particular, a comparison of the catalytic behavior with the phase composition of the bismuth–cerium molybdate system has yielded important insights into the solid state mechanism of selective olefin oxidation and ammoxidation by bismuth molybdate-containing catalysts.

EXPERIMENTAL

The catalysts were prepared by coprecipitation using aqueous solutions of $(NH_4)_6Mo_7O_{24} \cdot 4H_2O$, $(NH_4)_2Ce(NO_3)_6$, and $Bi(NO_3)_3 \cdot 5H_2O$. Other elements were added as their nitrate salts prior to coprecipitation. All the catalysts were supported on 20 wt% SiO_2 using an ammonium-stabilized silica sol. The slurry pH was adjusted to 3.0 by the addition of NH_4OH. The slurry was then evaporated to dryness with continual stirring. The catalysts were calcined at 290 and 425°C for 3 hr at each temperature. Most of the catalysts received a final calcination at 550°C for 16 hr. Select samples were calcined at 600 and 650°C in order to obtain a partial phase diagram for the system.

X-Ray powder patterns were obtained at 25°C using a Philips 50 kV universal vacuum spectrometer or Rigaku D/MAX-IIA X-ray diffractometer and Cu$K_{\alpha 1}$ radiation. Corundum (α-Al_2O_3) was used as an internal standard. Cell dimensions were obtained by least-squares treatment of the data.

Raman spectra were obtained with a Spex Ramalog 4 with a Spectra Physics 2 W argon ion laser.

Propylene ammoxidation experiments were conducted using a single pass, plug flow, tubular (3/8″ diameter) stainless-steel microreactor. The reactor was operated under atmospheric pressure at 420°C using a gaseous feed mixture consisting of a 1 : 1.2 : 10.5 : 4 molar mixture of propylene, ammonia, air, and water, respectively.

Pulse experiments were conducted using a pulse microreactor with an on-line Varian 3700 gc equipped with thermal conductivity and flame ionization detectors and a Houdry Micropak column system consisting of 36′ × 1/16″ molecular sieve 5A and 20″ × 1/16″ Porapak Q. Helium was used as the carrier gas with a flow rate of 30 cm^3/min over 1.0 cm^3 of catalyst. The pulse size was maintained at 37.35 μmole of a gaseous feed consisting of a 1 : 1.2 : 10 mixture of propylene, ammonia, and helium respectively.

RESULTS

Phase Composition of the $Bi_{2-x}Ce(MoO_4)_3$ System

Phase compositions of $Bi_{2-x}Ce_x(MoO_4)_3$ catalysts supported on silica and calcined

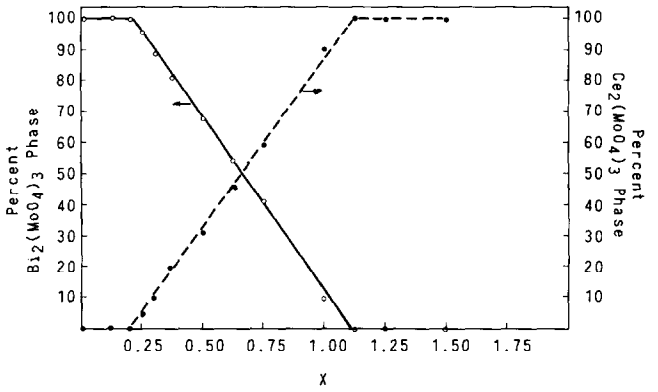

FIG. 1. Phase composition in the $Bi_{2-x}Ce_x(MoO_4)_3$ system after calcination at 550°C for 16 hr.

TABLE 1

Observed and Calculated *d*-Values for $Bi_{1.8}Ce_{0.2}(MoO_4)_3$ and $Bi_{0.5}Ce_{1.5}(MoO_4)_3$

$Bi_{1.8}Ce_{0.2}(MoO_4)_3$						$Bi_{0.5}Ce_{1.5}(MoO_4)_3$					
h	*k*	*l*	$d_{calc.}$	$d_{obs.}$	$I_{obs.}$	*h*	*k*	*l*	$d_{calc.}$	$d_{obs.}$	$I_{obs.}$
0	1	1	7.893	7.908	wm	−1	1	1	8.845	8.927	w
1	0	0	6.973	7.001	m	0	0	2	7.582	7.555	w
−1	1	1	6.286	6.282	wm	−2	0	2	6.658	6.637	w
1	1	0	5.969	5.966	w	0	2	1	5.111	5.528	wm
0	0	2	5.407	5.420	w	−1	1	3	4.861	4.874	wm
0	2	1	5.093	5.109	m	3	1	1	4.277	4.260	w
−1	2	1	4.574	4.584	w	−4	0	2	4.114	4.109	w
1	2	0	4.447	4.458	w	−1	1	4	3.776	3.771	w
−1	1	3	3.751	3.750	w	−3	1	4	3.525	3.526	w
0	3	1	3.626	3.637	wm	−4	2	3	3.180	3.183	vs
1	0	2	3.594	3.600	wm	−2	2	3	3.175	3.183	vs
1	1	2	3.432	3.430	w	0	4	0	2.958	2.958	s
2	1	0	3.338	3.347	wm	−1	3	4	2.803	2.806	w
−1	2	3	3.269	3.269	m	6	0	0	2.662	2.663	s
−2	2	1	3.191	3.194	vs	−2	4	3	2.326	2.328	w
0	2	3	3.058	3.064	vs	6	4	0	1.9785	1.9785	s
0	4	0	2.887	2.890	s	−8	0	6	1.8856	1.8862	m
−2	0	4	2.789	2.793	m	−4	0	6	1.8816	1.8802	m
−3	1	2	2.508	2.508	w	−4	6	3	1.7474	1.7454	m
2	0	2	2.487	2.487	wm	−10	2	3	1.6203	1.6203	m
−1	1	5	2.323	2.320	w	0	2	9	1.6203	1.6191	m
0	5	2	2.124	2.121	w	0	4	8	1.5959	1.5950	m
−2	4	4	2.006	2.005	m						
2	5	0	1.9253	1.9240	w						
4	0	−2	1.9147	1.9144	m						
2	4	2	1.8840	1.8826	m						
−4	1	4	1.8494	1.8484	w						
2	3	3	1.8423	1.8400	w						
0	0	6	1.8024	1.8038	wm						
−3	5	2	1.7177	1.7184	wm						
0	6	3	1.6977	1.6977	m						
−2	2	7	1.6376	1.6375	w						

at 550°C were determined from X-ray powder patterns (Fig. 1). All observed diffraction lines were unambiguously assigned to either $Bi_2(MoO_4)_3$ (*11*) or the low-temperature $La_2(MoO_4)_3$ (*9*) structure. At $x \leq 0.2$, the solid consists of single phase $Bi_2(MoO_4)_3$ indicating the presence of a solid solution of cerium in the bismuth molybdate lattice. At high cerium contents, where $x > 1$, the material is also single phase and crystallizes in the $La_2(MoO_4)_3$ structure. It is reported in the literature that $Ce_2(MoO_4)_3$ is isostructural with $La_2(MoO_4)_3$ (*7*), although our attempts to prepare single phase silica-supported $Ce_2(MoO_4)_3$ by coprecipitation and calcination between 550 and 750°C proved unsuccessful. Still higher calcination temperatures and absence of gaseous oxygen might be necessary to prepare this system. Nevertheless, the high cerium-containing compositions consist of a solid solution of bismuth dissolved in the $La_2(MoO_4)_3$ structure of cerium molybdate. At intermediate compositions with $0.2 < x < 1$, only mixtures of phases of the two end members were observed.

The observed and calculated *d* values for the most intense lines in the powder patterns of $Bi_{1.8}Ce_{0.2}(MoO_4)_3$ and $Bi_{0.5}Ce_{1.5}(MoO_4)_3$ are summarized in Table 1. These powder patterns were indexed by analogy to the monoclinic $Bi_2(MoO_4)_3$ and $La_2(MoO_4)_3$ structures, respectively. The agreement between the observed and calculated values is very good in both cases. The calculated cell parameters for the single phase bismuth–cerium molybdates are given in Table 2.

The phase composition of the $Bi_{2-x}Ce_x(MoO_4)_3$ system after calcination for 16 hr between 550 and 650°C is shown in Fig. 2. Calcination for 16 hr proved to be sufficient to achieve equilibrium solubility of the phases since calcination of selected samples at these temperatures for 3 to 5 days did not alter the distribution of the phases. From these results, it can be seen that the solubility of bismuth in cerium molybdate increases with temperature. Conversely, the solubility of cerium in the bismuth molybdate structure decreases at higher temperatures. No changes in lattice parameters as a function of calcination temperature were observed for the single phase materials.

The solubility of tungsten in the bismuth–cerium molybdate system was also examined since mutual solubility between various trivalent metal molybdates and tungstates has been observed (*12*). Typically, the rare earth molybdates and tungstates are not isostructural (*13, 14*). However, we observed that low levels of tungsten can be incorporated into the BiCe

TABLE 2

Lattice Parameters for $Bi_{2-x}Ce_x(MoO_4)_3$ and $BiCe(Mo_{1-z}W_zO_4)_3$ Solid Solutions

Composition[a]	Solvent phase	*a*(Å)	*b*(Å)	*c*(Å)	β (deg)	*V* (Å³)
$Bi_2(MoO_4)_3$	$Bi_2(MoO_4)_3$	7.718(2)	11.521(3)	11.979(3)	115.33(2)	962.7
$Bi_{1.975}Ce_{0.025}(MoO_4)_3$	$Bi_2(MoO_4)_3$	7.715(3)	11.530(4)	11.965(4)	115.26(3)	962.5
$Bi_{1.925}Ce_{0.075}(MoO_4)_3$	$Bi_2(MoO_4)_3$	7.706(2)	11.528(4)	11.966(4)	115.19(3)	961.9
$Bi_{1.875}Ce_{0.125}(MoO_4)_3$	$Bi_2(MoO_4)_3$	7.695(3)	11.531(4)	11.960(4)	115.24(3)	960.0
$Bi_{1.80}Ce_{0.20}(MoO_4)_3$	$Bi_2(MoO_4)_3$	7.710(4)	11.547(5)	11.957(6)	115.25(4)	962.7
$Bi_{1.75}Ce_{0.25}(MoO_4)_3$	$Bi_2(MoO_4)_3$	7.710(2)	11.544(3)	11.972(2)	115.31(2)	963.4
$BiCe(MoO_4)_3$	$Ce_2(MoO_4)_3$	16.801(7)	11.814(3)	16.061(9)	108.73(6)	3019
$Bi_{0.875}Ce_{1.125}(MoO_4)_3$	$Ce_2(MoO_4)_3$	16.839(8)	11.820(5)	16.022(9)	108.52(6)	3024
$Bi_{0.75}Ce_{1.25}(MoO_4)_3$	$Ce_2(MoO_4)_3$	16.844(8)	11.826(5)	16.011(9)	108.44(9)	3026
$Bi_{0.50}Ce_{1.50}(MoO_4)_3$	$Ce_2(MoO_4)_3$	16.841(8)	11.838(3)	16.024(9)	108.53(5)	3029
$BiCeMo_{2.5}W_{0.5}O_{12}$	$Ce_2(MoO_4)_3$	16.866(7)	11.819(3)	16.078(9)	109.21(6)	3026

[a] Supported on 20 wt% SiO_2.

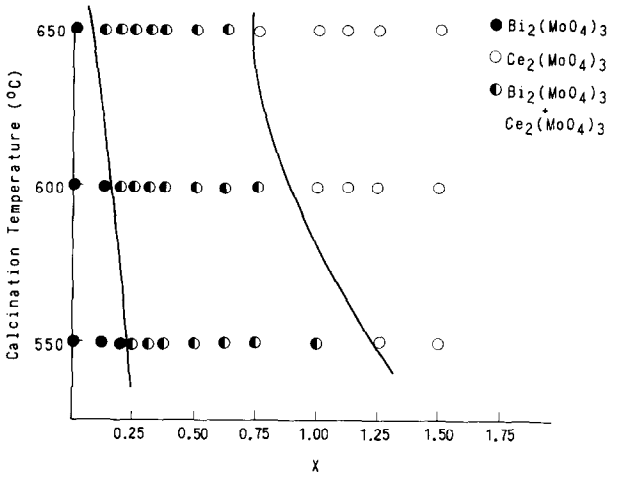

FIG. 2. Partial phase diagram for the $Bi_{2-x}Ce_x(MoO_4)_3$ system.

$(MoO_4)_3$ structure. Specifically, the X-ray powder pattern for $BiCeMo_{2.5}W_{0.5}O_{12}$ was readily indexed using the $La_2(MoO_4)_3$ structure with good agreement between observed and calculated *d* values. A comparison of the lattice parameters is given in Table 2. The incorporation of tungsten into the structure results in the preferential expansion of the cell along the *x* direction accompanied by an increase in the monoclinic angle, β, resulting in a small increase in the unit cell volume.

The maximum solubility of tungsten in the $BiCeMo_{3-z}W_zO_{12}$ structure occurs at approximately $z \simeq 0.75$. When the tungsten content is increased above this level, the X-ray powder patterns reveal the presence of a cerium tungstate phase of composition $Ce_4W_9O_{33}$ (ASTM Card File 25-192). At $z = 1.5$, the material is a complex mixture of $Ce_4W_9O_{33}$, Bi_2WO_6, and a bismuth–cerium molybdate solid solution.

Substitution by Other Rare Earth Elements

Since $La_2(MoO_4)_3$ and $Ce_2(MoO_4)_3$ are reported to be isostructural (*7*), we were interested to determine if the two molybdates are mutually soluble in the presence of bismuth. Therefore, several mixed molybdates were prepared with the composition $BiCe_{1-y}La_y(MoO_4)_3$ and their X-ray powder patterns were indexed by analogy to $La_2(MoO_4)_3$ with good agreement obtained between the observed and calculated *d*-values in all cases. The cell dimensions are given in Table 3 and the change in cell volume as a function of catalyst composition is shown in Fig. 3. The formation of a continuous solid solution between La- and Ce–molybdate is demonstrated by the linear change in the cell volume as the La/Ce ratio is varied, indicating a random replacement of cerium cations by lanthanum in the structure.

It was also found that cerium can be replaced by other large trivalent cations without destroying the integrity of the $La_2(MoO_4)_3$ structure. Mixed molybdates with the formula $BiCe_{0.5}M_{0.5}(MoO_4)_3$ where M = Y, Nd, Pr, and La were prepared and their X-ray powder patterns were readily indexed by analogy to lanthanum molybdate.

TABLE 3

Lattice Parameters for the $BiCe_{1-y}La_y(MoO_4)_3$ System

y	*a* (Å)	*b* (Å)	*c* (Å)	β (deg)	*V* (Å^3)
0	16.801(7)	11.814(3)	16.061(9)	108.73(6)	3019
0.25	16.857(2)	11.830(2)	16.007(7)	108.51(2)	3027
0.50	16.884(2)	11.836(2)	16.071(6)	108.83(2)	3040
0.75	16.880(2)	11.839(3)	16.084(8)	108.68(2)	3045
1.00	16.894(4)	11.866(3)	16.094(6)	108.92(4)	3052

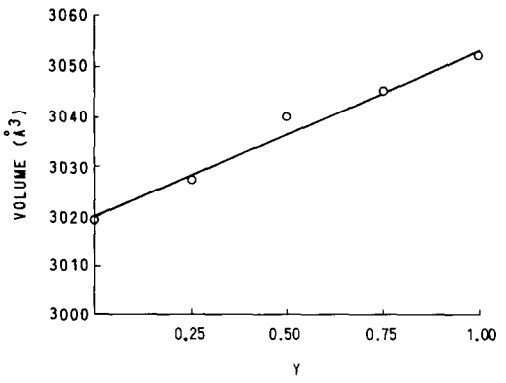

FIG. 3. Change in cell volume with composition for $BiCe_{1-y}La_y(MoO_4)_3$.

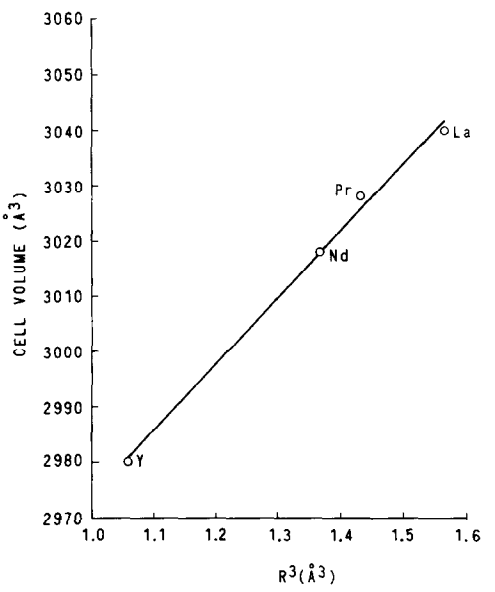

FIG. 4. Change in cell volume as a function of the cube of the ionic radii of the substituting cation M in $BiCe_{0.5}M_{0.5}(MoO_4)_3$.

The lattice parameters for the rare-earth containing Bi–Ce molybdates are summarized in Table 4 and the calculated cell volumes are plotted in Fig. 4 as a function of the cube of the ionic radii of the substituting cations. Ionic radii for eight coordinated cations given by Shannon (*15*) are used in the figure. Clearly, all the large trivalent cations investigated can readily occupy the cation sites of the $La_2(MoO_4)_3$ structure. The incorporation of Pr and Nd into this structure is not surprising since they both form isostructural molybdates with $La_2(MoO_4)_3$. Conversely, $Y_2(MoO_4)_3$ is reported to crystallize in the $Sc_2(WO_4)_3$ structure which is characterized by six coordination of the trivalent cation and tetrahedral coordination of the hexavalent cation (*16*). Nevertheless, there appears to be sufficient driving force for the mixed Bi–Ce–Y–molybdate to crystallize in the $La_2(MoO_4)_3$ structure although in this series the cerium comprises only 25% of the trivalent elements. A somewhat similar result was reported by Nassau *et al.* (*13*) for mixed trivalent tungstates containing cerium. They observed that $CeY(WO_4)_3$ crystallizes with the same structure as $Ce_2(WO_4)_3$ even though cerium tungstate is not isostructural with $Y_2(WO_4)_3$.

TABLE 4

Lattice Parameters for the $BiCe_{0.5}M_{0.5}(MoO_4)_3$ System

M	*a* (Å)	*b* (Å)	*c* (Å)	β (deg)	*V* (Å^3)
La^{3+}	16.884(2)	11.836(2)	16.071(6)	108.83(2)	3040
Pr^{3+}	16.829(2)	11.809(2)	16.102(6)	108.86(2)	3028
Nd^{3+}	16.829(2)	11.780(3)	16.131(5)	109.30(2)	3018
Y^{3+}	16.744(5)	11.758(3)	16.030(9)	109.21(3)	2980

In addition, compositions were prepared in which lanthanum partially replaced either bismuth or bismuth and cerium: $Bi_{1-y}La_yCe(MoO_4)_3$ and $Bi_{1-y}Ce_{1-y}La_{2y}Mo_{2.5}W_{0.5}O_{12}$. The calculated lattice parameters for these compositions are given in Table 5. Cell volume increases linearly with the cube of the averaged cation radii when lanthanum is substituted for both bismuth and cerium in the lattice (Fig. 5). Therefore, isomorphous replacement of both cerium and bismuth by lanthanum is strongly indicated. There is virtually no observed change in cell volume when lanthanum is substituted for bismuth alone (Table 5) which may be expected based on the similarity in the ionic radii of 8-coordinated Bi^{3+} and La^{3+} (*15*).

TABLE 5

Lattice Parameters for $Bi_{1-y}Ce_{1-y}La_{2y}Mo_{2.5}W_{0.5}O_{12}$ and $Bi_{1-y}La_yCe(MoO_4)_3$

Composition	a (Å)	b (Å)	c (Å)	β (deg)	V (Å³)
$Bi_{0.75}Ce_{0.75}La_{0.5}Mo_{2.5}W_{0.5}O_{12}$	16.915(2)	11.833(2)	16.126(4)	109.21(2)	3048
$Bi_{0.5}Ce_{0.5}La_1Mo_{2.5}W_{0.5}O_{12}$	16.953(2)	11.898(2)	16.011(4)	108.94(2)	3051
$Bi_{0.25}Ce_{0.25}La_{1.5}Mo_{2.5}W_{0.5}O_{12}$	16.939(2)	11.891(2)	16.039(4)	109.00(2)	3055
$Bi_{0.5}La_{0.5}Ce(MoO_4)_3$	16.868(2)	11.871(2)	16.069(3)	108.69(2)	3048
$Bi_{0.25}La_{0.75}Ce(MoO_4)_3$	16.924(3)	11.852(2)	16.051(4)	108.85(2)	3047

Raman Spectroscopic Analysis

Raman spectra of the bismuth–cerium molybdates and of lanthanum–molybdate are summarized in Table 6. In general, few shifts in band positions can be seen as the Bi/Ce content is changed. The high frequency band at 953 cm^{-1} in $Bi_2(MoO_4)_3$, which is assigned to the Mo=O moiety in the structure, decreases in intensity with increasing cerium content. This band is absent at high cerium contents where the material is a single phase solid solution of bismuth in the cerium molybdate lattice. This is consistent with the Raman spectrum of the isostructural $La_2(MoO_4)_3$ which shows no evidence of Mo=O in the structure.

The Raman bands above 800 cm^{-1} have been assigned to the vibrational modes of the MoO_4 tetrahedra (*17*). The only significant shift in this region is the 921 cm^{-1} band of bismuth molybdate which moves to lower frequencies as the cerium content is increased. Poorly resolved bands at 925 and 884 cm^{-1} also become apparent at the highest cerium levels.

Catalytic Activity

The effectiveness of bismuth–cerium molybdates as catalysts for selective propylene ammoxidation to acrylonitrile was examined under both continuous flow and pulse microreactor conditions. The overall catalytic activity as a function of catalyst composition is shown in Fig. 6. Three distinct activity maxima are observed as the Bi/Ce ratio is varied in the $Bi_{2-x}Ce_x(MoO_4)_3$ system. The propylene conversion maxima occur at x = 0.20, 0.375 and 1.125. The surface area of all the silica-supported bismuth–cerium molybdates is nearly the same (Fig. 6) and does not account for the differences in catalytic activity. Hence, the observed activity differences are clearly fundamentally related to the solid state structure and chemistry of these materials.

The observed relationship between catalytic behavior was confirmed by pulse microreactor experiments. Figure 7 shows the propylene conversion and acrylonitrile yield for several of the bismuth–cerium molybdates when pulsed with a propylene, ammonia, and helium mixture in the ab-

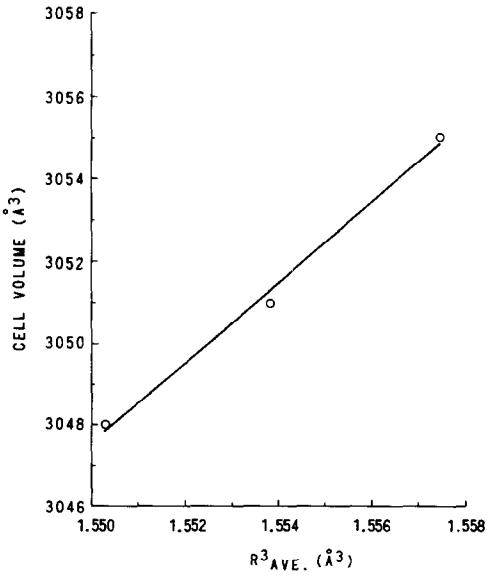

FIG. 5. Change in cell volume as a function of the cube of the average ionic radii in $Bi_{1-y}Ce_{1-y}La_{2y}Mo_{2.5}W_{0.5}O_{12}$ compositions.

TABLE 6

Raman Spectra of the $Bi_{2-x}Ce_x(MoO_4)_3$ System[a]

$Bi_2(MoO_4)_3$	$Bi_{1.75}Ce_{0.25}(MoO_4)_3$	$Bi_{1.7}Ce_{0.3}(MoO_4)_3$	$Bi_{1.5}Ce_{0.5}(MoO_4)_3$	$Bi_{1.25}Ce_{0.75}(MoO_4)_3$	$BiCe(MoO_4)_3$	$Bi_{0.5}Ce_{1.5}(MoO_4)_3$	$La_2(MoO_4)_3$
953_{12}	952_9	954_{10}	952_8	954_6			944_{46}
					930_{47}	925_{58}	934_{22}
921_{38}	918_{35}	914_{46}	912_{49}	910_{76}	910_{112}	910_{155}	915_{73}
898_{100}	897_{100}	895_{100}	896_{100}	898_{100}	898_{100}	898_{100}	897_{100}
						884_{94}	862_{14}
855_{24}	853_{20}	852_{24}	852_{27}	855_{30}	855_{38}	855_{40}	852_{15}
838_{23}	838_{19}	834_{23}	834_{24}	834_{30}	830_{41}		823_{62}
813_{42}	812_{32}	810_{27}	811_{30}	814_{35}	818_{42}	818_{53}	808_{52}

[a] Band positions reported in cm^{-1}. Relative intensities of the bands are noted as subscripts.

sence of gaseous oxygen. Both the catalytic activity and acrylonitrile yield are maximum in the composition regions where maximum catalytic activity was observed in the continuous flow microreactor experiments.

The redox properties of $BiCe(MoO_4)_3$ and $Bi_{0.5}Ce_{1.5}(MoO_4)_3$ were also examined in the pulse reactor. The catalysts were sequentially pulsed with a mixture of propylene, ammonia, and helium at 420°C resulting in the progressive depletion of oxygen from the lattice. The observed changes in propylene conversion and acrylonitrile selectivity are shown in Fig. 8. For both catalysts, the propylene conversion declined sharply after the first few pulses, while the selectivity to acrylonitrile decreased only slightly, leveling off at about 70% in both cases.

The higher overall activity of $BiCe(MoO_4)_3$ indicates that this catalyst possesses a larger number of active and accessible lattice oxygens, as well as a superior mechanism for regeneration and reoxidation of the surface active sites by lattice oxygen anions. In addition, the $BiCe(MoO_4)_3$ catalyst is more redox stable than the $Bi_{0.5}Ce_{1.5}(MoO_4)_3$ composition since the overall performance of the $BiCe(MoO_4)_3$ catalyst is unchanged or slightly improved after reduction and reoxidation in flowing air at 420°C. However, the acrylonitrile selectivity of the $Bi_{0.5}Ce_{1.5}(MoO_4)_3$ catalyst is initially lower after reoxidation, increases with partial reduction, but rapidly deteriorates with further depletion of lattice oxygen, even though the original activity of the catalyst is restored by reoxidation.

DISCUSSION

Solid State Structural Aspects of the $Bi_{2-x}Ce_x(MoO_4)_3$ System

Since the end members of the $Bi_2(MoO_4)_3$–$Ce_2(MoO_4)_3$ system are not isostructural, only partial solid solubility is expected. The partial phase diagram of this system (Fig. 2) reveals two regions of solid

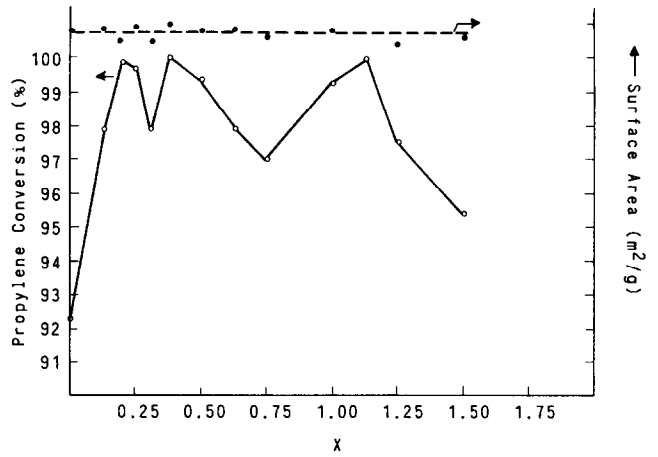

FIG. 6. Catalytic activity and surface area for the $Bi_{2-x}Ce_x(MoO_4)_3$ system. Catalytic activity was measured using a feed mixture of propylene : ammonia air : water = 1 : 1.2 : 10.5 : 4.0 at 420°C in a continuous flow microreactor.

solution formation with partial solubility at both the bismuth-rich and cerium-rich compositions. The extent of solid solubility of the two phases is not expected to be hindered by the need for the cations to undergo any change in coordination since both bismuth and cerium are eight coordinated by oxygen in both molybdate structures. Therefore, the most important factor in determining solid solubility will be cation size and its effect on the ordering of cation vacancies.

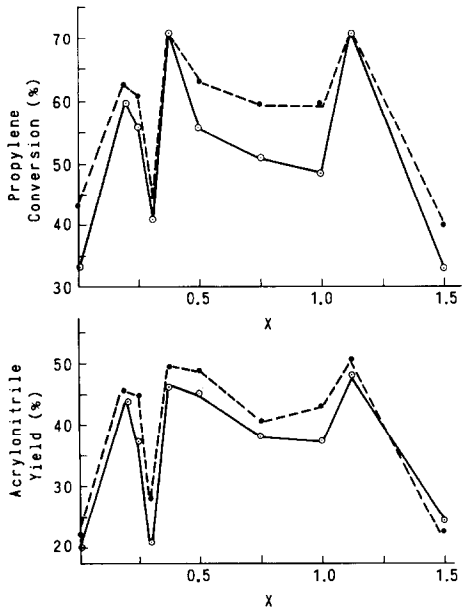

FIG. 7. Pulse catalytic ammoxidation of propylene as a function of catalyst composition for the $Bi_{2-x}Ce_x(MoO_4)_3$ system using fresh catalyst (——) and reduced and reoxidized catalyst (----) at 420°C. Feed: propylene : ammonia : helium = 1 : 1.2 : 10. Pulse size = 37.35 μmole.

From the ionic radii given by Shannon (*15*) (Bi^{3+} = 1.17 Å, Ce^{3+} = 1.143 Å) the incorporation of bismuth and cerium in the same structure appears possible. However, Bi^{3+} cations possess lone pairs of electrons ($6s^2$) which cause considerable distortion of the $Bi_2(MoO_4)_3$ structure (*9*). This lone pair effect generates Mo_2O_8 dimers (*6*) rather than the discrete MoO_4 tetrahedra present in the $La_2(MoO_4)_3$ structure. Such structural distortion is also evident in the $Bi_{2-x}Ce_x(MoO_4)_3$ system. Figure 9 shows the change in cell volume for both the bismuth-rich and cerium-rich solid solutions as a function of the relative Bi/Ce content. When the amount of bismuth dissolved in the $Ce_2(MoO_4)_3$ lattice is sufficient for the existence of neighboring bismuth cations in the structure, the resulting lone pair effect causes MoO_4 pairs to coalesce. This contraction produces an overall decrease in cell volume. Conversely, when the cerium

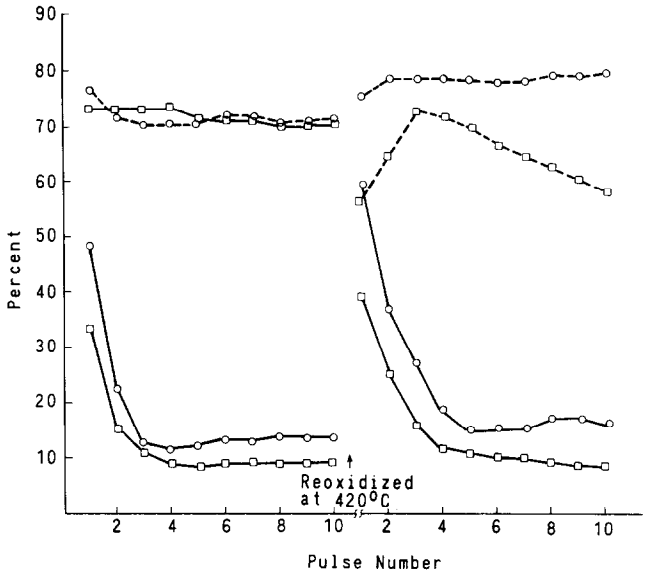

FIG. 8. Propylene conversion (——) and acrylonitrile selectivity (---) as a function of pulse number for (○) $BiCe(MoO_4)_3$ and (□) $Bi_{0.5}Ce_{1.5}(MoO_4)_3$ at 420°C. Feed = propylene : ammonia : helium = 1 : 1.2 : 10. Pulse size = 37.35 μmole.

content in the $Bi_2(MoO_4)_3$ structure is sufficiently large, the generation of discrete MoO_4 tetrahedra from Mo_2O_8 dimers expands the unit cell.

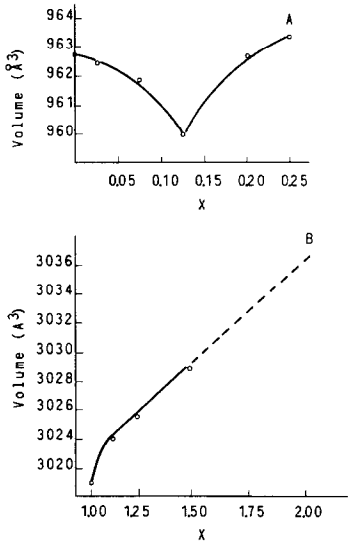

FIG. 9. Change in cell volume with composition in the $Bi_{2-x}Ce_x(MoO_4)_3$ system for (A) bismuth-rich and (B) cerium-rich solid solutions.

In the region where isolated bismuth or cerium cations are present in the host lattice, changes in the unit cell volume reflect the relative sizes of the Bi^{3+} and Ce^{3+} cations. This is indicated for dilute solid solutions of cerium in bismuth molybdate by a cell volume decrease with increasing cerium content (Fig. 9A). Also, the reported unit cell volume of $Ce_2(MoO_4)_3$ (7) (3032.7 Å^3) is less than that expected from an extrapolation of the observed change in cell volume with increased cerium content in the cerium-rich solid solution (Fig. 9B).

From the partial phase diagram (Fig. 2), it is clear that the extent of the solubility of bismuth in the $Ce_2(MoO_4)_3$ structure is much larger than that of cerium in $Bi_2(MoO_4)_3$. The solubility limit of Ce in $Bi_2(MoO_4)_3$ occurs at about 10 mole% $Ce_2(MoO_4)_3$ at 550°C and decreases with increasing temperature. Conversely, the solubility limit of Bi in $Ce_2(MoO_4)_3$ is about 50 mole% at 550°C and increases with temperature. These observed changes in solid solubility with temperature can be used to estimate relative partial molal enthalpies

for the individual components using the following expressions (18):

$$\frac{X_{Ce}^{(Bi\text{-}Mo)}\,(sat)}{X_{Ce}^{(Ce\text{-}Mo)}\,(sat)} = A \exp. - \left(\frac{\Delta\bar{H}_{Ce}^{(Bi\text{-}Mo)}}{RT}\right) \quad (1)$$

$$\frac{1 - X_{Ce}^{(Ce\text{-}Mo)}\,(sat)}{1 - X_{Ce}^{(Bi\text{-}Mo)}\,(sat)} = B \exp. - \left(\frac{\Delta\bar{H}_{Bi}^{(Ce\text{-}Mo)}}{RT}\right) \quad (2)$$

where X_A^{β} (sat) is the solubility limit of A in phase β at a given temperature and $\Delta\bar{H}_A^{\beta}$ is the relative partial molal enthalpy of A in β. The data are plotted in Fig. 10 for both the bismuth-rich and cerium-rich solid solutions. From the slopes of the resulting straight lines, the following values for the relative partial molal enthalpies are obtained:

$$\Delta\bar{H}_{Ce}^{(Bi\text{-}Mo)} = -9.5 \text{ kcal/mole}$$

and

$$\Delta\bar{H}_{Bi}^{(Ce\text{-}Mo)} = 3.3 \text{ kcal/mole.}$$

The larger enthalpy necessary to transfer bismuth from the pure $Bi_2(MoO_4)_3$ to the $Ce_2(MoO_4)_3$ phase may be a consequence of the lone pair effect discussed above. The excellent fit of the experimental data to Eqs. (1) and (2) confirms that these materials have indeed achieved their equilibrium solubility at each calcination temperature.

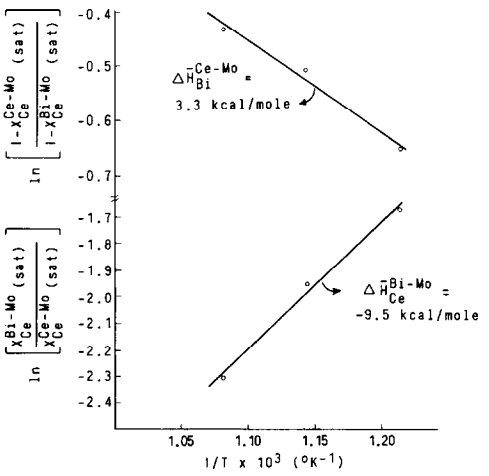

FIG. 10. Partial molal enthalpies for $Bi_2(MoO_4)_3$–$Ce_2(MoO_4)_3$ solid solutions according to Eqs. (1) and (2).

The data discussed so far show that the cerium-rich bismuth–cerium molybdates crystallize as single phase materials which are isostructural with $La_2(MoO_4)_3$. In addition cerium can be replaced by other large trivalent rare earth cations as evidenced by the linear change in cell volume reflecting the size of the substituting cation (Fig. 4). However, from these results it is not possible to determine whether any ordering of bismuth or cerium cations takes place in the structure or whether a random solid solution exists. To resolve this question, X-ray powder patterns of $Bi_{1-y}La_yCe(MoO_4)_3$ and $Bi_{1-y}Ce_{1-y}La_yMo_{2.5}W_{0.5}O_{12}$ systems were examined.

The observed changes in unit cell volume were correlated to the average ionic radii of the three cations present at each composition studied. The resulting linear correlation indicates that bismuth and cerium are replaced by lanthanum in the structure with equal probability (Table 5 and Fig. 5). This strongly suggests that bismuth and cerium randomly occupy equivalent cation positions in the scheelite $La_2(MoO_4)_3$ structure. Single crystal studies are in progress to determine the exact cation positions of these complex solid solutions.

Relationship between Catalytic Behavior and Solid State Structure

The catalytic activity of a silica-supported cerium-doped bismuth molybdate catalyst with a composition of $Bi_9Ce_1Mo_{12}O_{52}$ was reported by Giordano and Bart (*4*). However, no structural information was given about the catalyst, nor was there any discussion concerning the role of cerium in the catalytic process. Our study of the bismuth–cerium molybdate system reveals that cerium is effective in increasing the overall activity of bismuth molybdate catalysts. In addition, there are unique compositions where catalytic activity is

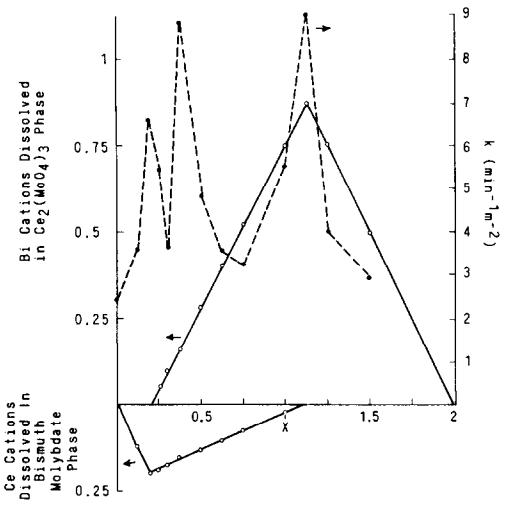

FIG. 11. Cation solubility (——) and first-order rate constant (---) for the $Bi_{2-x}Ce_x(MoO_4)_3$ system as a function of composition. Rate constants were calculated from the rate of propylene disappearance at 420°C.

maximized and these compositions correspond to specific features in the phase diagram.

The reasons for the uniqueness of these compositions can be seen from Fig. 11, which shows the cation solubility and catalytic activity as a function of the bulk composition. The high catalytic activity in $Bi_{2-x}Ce_x(MoO_4)_3$ at $x = 0.2$ and 1.125 corresponds to the solubility limits of the two respective single phase systems at 550°C. At $x = 0.2$ maximum solubility of cerium cations in the bismuth molybdate phase is achieved, while the maximum solubility of bismuth cations in cerium molybdate is obtained at $x = 1.125$. The high catalytic activity of these compositions results from the coexistence of bismuth and cerium cations in a single molybdate structure. This intimate mixing of key catalytic components in a single solid state structure is a very important feature of an effective oxidation catalyst. The single solid state structure acts as a host and template to keep these components in close proximity to each other, both at the surface and in the bulk.

These results further confirm our earlier mechanistic studies (*19*) that in bismuth molybdate-based catalysts, the presence of bismuth–molybdenum pairs is required for selective oxidation and ammoxidation of olefins. The molybdenum in this two-component bifunctional active site serves as a coordinately unsaturated center for olefin chemisorption and selective oxygen or nitrogen insertion. Bismuth is necessary to activate the olefin via α-H abstraction in the rate-determining step and to produce the allylic intermediate.

The enhanced catalytic activity obtained by the addition of cerium to bismuth molybdate is not due to an increase in the number of the α-H abstracting centers. Cerium molybdate is neither as active nor as selective as bismuth molybdate for propylene ammoxidation (e.g., approximately 25% propylene conversion with about 15% selectivity to acrylonitrile at comparable reaction conditions). In addition, the lack of any definitive correlation between the Raman band positions and catalytic behavior indicates that the presence of cerium does not significantly alter the metal–oxygen bond strength of the MoO_4 polyhedra. Instead, the role of cerium is similar to that of iron in the $Bi_3FeMo_2O_{12}$ catalyst (*20*). Like iron, cerium is a multivalent cation capable of facile redox and can thereby aid in the reoxidation and reconstruction of the surface active sites (i.e., Bi–Mo sites). Assigning cerium primarily a redox role has precedent in the Te–Mo oxide-based catalysts where cerium has been shown to enhance the reoxidation rate and thus substantially decrease the reductive deactivation of that catalyst system (*21*).

Our results illustrate clearly that high catalytic activity is achieved in the $Bi_{2-x}Ce_x(MoO_4)_3$ system when the greatest number of the three components (Bi, Ce, Mo) can coexist and interact in a single solid state structure. This is evidenced by several experimental facts: (i) the $Bi_{0.875}Ce_{1.125}(MoO_4)_3$ solid solution is more active than the $Bi_{1.8}Ce_{0.2}(MoO_4)_3$ solid solution (Fig. 7) and (ii) the $BiCe(MoO_4)_3$ composition possesses a

larger reservoir of active oxygens and is more redox stable than $Bi_{0.5}Ce_{1.5}(MoO_4)_3$ (Fig. 8). Also, since the X-ray powder data reveal that the bismuth–cerium molybdate solid solutions are random, catalysts which are either bismuth rich or cerium rich will possess less than optimum interactive bismuth–cerium neighbors. Such catalysts will therefore have surface regions whose catalytic activity is not markedly different from that of either pure bismuth molybdate or cerium molybdate.

Variations in catalytic activity as a function of the Bi/Ce ratio were also observed in the two phase region of the $Bi_{2-x}Ce_x(MoO_4)_3$ system. Based on X-ray diffraction data, the high catalytic activity of the $Bi_{1.625}Ce_{0.375}(MoO_4)_3$ composition is not the result of a new separate phase. The data strongly suggest that at $x = 0.375$ there exists a true binary solid solution consisting of about 80 mole% $Bi_{1.8}Ce_{0.2}(MoO_4)_3$ and 20 mole% $Bi_{0.875}Ce_{1.125}(MoO_4)_3$.

High catalytic activity in multicomponent–multiphase systems is certainly not unprecedented (*22*). Many industrially important catalyst systems owe their high activity and selectivity to interfacial effects between structurally different phases. For example, Wolfs and Batist (*23*) investigated multicomponent catalysts of the type $M^{2+}M^{3+}BiMo_{12}O_x$ and attributed high catalytic activity and selectivity to interactions between three different molybdate phases. Margolis and co-workers (*24*) have interpreted the catalytic properties of this system by an interaction model wherein the active centers are situated at the interfaces between different phases.

In the multiphase region of bismuth–cerium molybdates, the catalytic activity depends on the distribution of bismuth and cerium at the surface and at the phase boundaries. For $Bi_{1.625}Ce_{0.375}(MoO_4)_3$ the observed phase composition is nearly that expected of an ideal mixture of separate $Bi_2(MoO_4)_3$ and $Ce_2(MoO_4)_3$ phases. Therefore, at this composition equal amounts of bismuth and cerium are dissolved in the cerium molybdate and bismuth molybdate phases, respectively (Fig. 11). As a consequence, no shift in the phase boundary is necessary during final calcination.

For all other compositions of the two phase region, the catalyst precursors contain more bismuth molybdate or cerium molybdate phase than is present after final calcination. A shift in the phase boundary therefore must occur during the calcination and unequal amounts of bismuth or cerium dissolve in the cerium molybdate or bismuth molybdate phases, respectively (Fig. 11). This can result in large and diffuse phase boundaries having nonequilibrium compositions (*25, 26*). Thus, compared to the $Bi_{1.625}Ce_{0.375}(MoO_4)_3$ catalyst, such compositions may contain larger amounts of material with nonequilibrium compositions. Because of the resulting nonoptimal distribution of key catalytic components, these compositions have, as expected, lower catalytic activity than either of the optimum equilibrium solid solutions or the two phase $Bi_{1.625}Ce_{0.375}(MoO_4)_3$ composition. A detailed investigation of the structure and composition of interfaces of these catalytic materials will be reported in a forthcoming paper.

CONCLUSIONS

Mixed bismuth–cerium molybdates are active catalysts for the selective ammoxidation of propylene to acrylonitrile. A detailed examination of their catalytic behavior and solid state structure reveals that high catalytic activity is achieved in compositional regions of maximum mutual solid solubility. In these regions, maximum atomic dispersion of Ce and Bi in molybdate matrices is realized. This optimizes catalytic efficiency because of optimized proximity of all three key catalytic elements: Mo (propylene chemisorbing and nitrogen inserting element), Bi (α-H abstracting element), and Ce (oxygen and electron transfer element). The enhancement in catalytic activity over the end members results from an increase in the oxygen ion, elec-

tron, and anion vacancy transport due to the presence of the facile $Ce^{3+} \rightleftharpoons Ce^{4+}$ redox couple operating in a solid state oxide matrix containing the two essential elements Bi and Mo of the active and selective bifunctional catalyst site. The reconstruction rate of these sites and, therefore, their time averaged number effectively working at the surface is, thus, substantially enhanced.

ACKNOWLEDGMENTS

We wish to thank Professor E. Kostiner of the University of Connecticut, and Dr. M. A. Tenhover for their many helpful discussions. We also acknowledge the assistance of Dr. M. Mehicic and Mrs. M. A. Hazle for obtaining the Raman spectra, and Mr. R. A. Gerron and Mr. E. Wong for the X-ray powder diffraction data.

REFERENCES

1. Brixner, L. H., Barkley, J. R., and Jeitschko, W., *in* "Handbook on the Physics and Chemistry of Rare Earths" (K. A. Gschneider and L. Eyring, Eds.). North Holland Publishing, Amsterdam, 1979.
2. Callahan, J. L., Grasselli, R. K., Milberger, E. C., and Strecker, H. A., *I&EC Prod. Res. Dev.* **9,** 134 (1970).
3. Grasselli, R. K., and Burrington, J. D., *Adv. Catal.* **30,** 133 (1981).
4. Giordano, N., and Bart, J. C. J., *Recl. Trav. Chim. Pays-Bas* **94,** 28 (1975).
5. Otaki, T., Hatano, M., Koyama, T., and Oshima, K. (Mitsubishi Chemical Industries Co.), *Japan Kokai Tokkyo Koho* **79,** 124, 885.
6. Van den Elzen, A. F., and Rieck, G. D., *Acta Crystallogr. B* **29,** 2433 (1973).
7. Brixner, L. H., Sleight, A. W., and Licis, M. S., *J. Solid State Chem.* **5,** 247 (1972).
8. Brixner, L. H., *Rev. Chim. Min.* **10,** 47 (1973).
9. Jeitschko, W., *Acta Crystallogr. B* **29,** 2074 (1973).
10. Trifiro, F., Pasquon, I., and Centola, P., *J. Catal.* **10,** 86 (1968).
11. Aykan, K., *J. Catal.* **12,** 281 (1968).
12. Nassau, K., Shiever, J. W., and Keve, E. T., *J. Solid State Chem.* **3,** 411 (1971).
13. Nassau, K., Lebinstein, H. J., and Loiacono, G. M., *J. Phys. Chem. Solids* **26,** 1805 (1965).
14. Brixner, L. H., and Sleight, A. W., *Mat. Res. Bull.* **8,** 1269 (1973).
15. Shannon, R. D., *Acta Crystallogr. A* **32,** 751 (1976).
16. Jamieson, P. B., Abrahams, S. C., and Bernstein, J. L., *J. Chem. Phys.* **50,** 86 (1969).
17. Matsuura, I., Schut, R., and Hirakawa, K., *J. Catal.* **63,** 152 (1980).
18. Swalin, R. A., "Thermodynamics of Solids," p. 177. Wiley, New York, 1972.
19. Grasselli, R. K., Burrington, J. D., and Brazdil, J. F., *Faraday Disc.* **72,** 203 (1982).
20. Brazdil, J. F., Suresh, D. D., and Grasselli, R. K., *J. Catal.* **66,** 347 (1980).
21. Bart, J. C. J., and Giordano, N., *J. Catal.* **64,** 356 (1980).
22. Grasselli, R. K., and Hardman, H. F., U.S. Patent 3,642,930 (1972); Grasselli, R. K., Suresh, D. D., and Hardman, H. F., U.S. Patent 4,001,317 (1977), U.S. Patent 4,139,552 (1979); Grasselli, R. K., Suresh, D. D., and Miller, A. F., U.S. Patent 4,167,494 (1979).
23. Wolfs, M. W. J., and Batist, Ph, A., *J. Catal.* **32,** 25 (1974).
24. Vorob'eva, G. A., Rozentuller, B. V., Maksimov, Yu. V., Kutyrev, M. Yu., and Margolis, L. Ya, *J. Catal.* **71,** 405 (1981).
25. Ref. (*18*), pp. 237–239.
26. Cahn, J. W., and Hilliard, J. E., *J. Chem. Phys.* **28,** 258 (1958).